

Yield Stress Dependency on the Evolution of Bubble Populations Generated in Consolidated Soft Sediments

Michael Johnson , Michael Fairweather, David Harbottle, and Timothy N. Hunter

School of Chemical and Process Engineering, University of Leeds, Leeds LS2 9JT, U.K.

Jeffrey Peakall

School of Earth and Environment, University of Leeds, Leeds LS2 9JT, U.K.

Simon Biggs

School of Chemical Engineering, University of Queensland, Brisbane, QLD 4072, Australia

DOI 10.1002/aic.15731

Published online May 2, 2017 in Wiley Online Library (wileyonlinelibrary.com)

Retention of hydrogen bubbles within consolidated soft sediments represents an important safety consideration for the management of legacy nuclear wastes due to the potential for acute gas release. Gas retention sufficiently reduced the bulk density of intermediate yield stress (<800 Pa) sediments for the bed to become buoyant with respect to an aqueous supernatant, potentially inducing Rayleigh-Taylor instabilities. X-ray computed tomography revealed that beds of 7–234 Pa yield stress retained very similar, steady state size distributions of mature bubbles, limited to 9 mm equivalent spherical diameter, for long residence times. This implied a dominant gas release mechanism dictated by the pore to millimeter scale bubble population, not previously identified in such weak sediments and unrelated to the bubbles' buoyant force. At 1112 Pa yield stress, large bubbles of up to 20 mm diameter were observed to grow through induction of lateral cracks, facilitating gas transport to the bed periphery, thereby limiting the maximum void fraction, while non-homogeneous gas generation promoted the formation of low density regions rich with microbubbles which similarly provide pathways for gas release. © 2017 The Authors AICHE Journal published by Wiley Periodicals, Inc. on behalf of American Institute of Chemical Engineers AICHE J, 63: 3728–3742, 2017

Keywords: gas retention, x-ray tomography, yield stress, nuclear waste

Introduction

In situ bubble generation and retention is frequently encountered in various natural water systems, such as biogenic methane within shallow marine beds,^{1–5} lake bottoms,^{6,7} river estuaries,⁸ dredging sludge,⁹ and anaerobic digesters.¹⁰ Hydrogen bubble retention also represents a major consideration for the management of intermediate level waste (ILW) streams at legacy nuclear waste facilities, for example, at Sellafield, UK and Hanford, USA.^{11–14} Hydrogen is generated by the corrosion of first generation cladding materials such as aluminium and the Magnox alloy,^{15,16} while hydrogen and methane are also produced by radiolysis reactions, often initiating with the radioactive decay of water soluble fission products such as cesium and strontium.^{14,15}

The study of bubbles in concentrated mineral suspensions, or consolidated *soft sediments*, poses many challenges for researchers. Their mechanical response during bubble growth is governed by complex functions of sediment strength,^{1,9,14,17}

microstructure^{5,12,13,18–21} and three phase wetting behavior.^{11,20,22,23} Concentrated mineral suspensions found in mining tailings,²⁴ wastewater slurries,²⁵ and nuclear sludge²⁶ exhibit a complex, non-Newtonian response to stress, typified by shear thinning characteristics, a shear and compressive yield stress and sometimes thixotropic behavior.^{27,28} While a yield stress is most commonly associated with viscoplastic behavior, creep tests have shown that flocculated mineral suspensions exhibit a *viscoelastic* response to a broad range of shear stress conditions.^{29,30} Furthermore, many soft sediments are also highly heterogeneous in nature^{16,31} and so exhibit significant spatial variation in mechanical properties such as compressive and shear yield stress, Young's modulus and Poisson ratio. The local mechanical properties of the sediment are also influenced by the presence of gas bubbles^{17,32,33} and hysteresis effects due to disturbance of the bed during bubble release.¹⁸ Consequently, no rheological model describing the mechanical response of viscoelastic, porous sediments during bubble growth has been widely accepted.²

Progress in this field has in part been limited by the opaque nature of soft sediments which rules out optical microscopy for investigating the size, geometry, and dynamics of retained bubbles.³⁴ However, x-ray computed tomography (CT) has been used in a handful of studies,^{2,34–38} revealing various void geometries, such as cornflake,^{2,34} inverted teardrop³⁹ and disk-shaped bubbles,³⁸ under different viscoelastic conditions. Bubbles

Correspondence concerning this article should be addressed to Michael Johnson at pm12mcj@leeds.ac.uk.

This is an open access article under the terms of the Creative Commons Attribution License, which permits use, distribution and reproduction in any medium, provided the original work is properly cited.

© 2017 The Authors AICHE Journal published by Wiley Periodicals, Inc. on behalf of American Institute of Chemical Engineers

quickly grow to the scale of pores or capillaries within soft sediments, at which point the bubble encounters the sediment matrix and the mechanics of bubble growth will depart from those in conventional fluids.³⁴ A number of mechanisms have been proposed for subsequent bubble growth under different sediment strength, wettability, and microstructure conditions³⁴:

- *Capillary invasion* occurs when the growing bubble encounters the sediment matrix and the sediment structure remains rigid, forcing the bubble to intrude into the dendritic pore network. Capillary invasion is governed by the Young-Laplace equation,⁴⁰ which implies that soft sediments with small grain sizes and correspondingly small pore throat radii will resist capillary invasion due to the high pore entry pressures. Likewise, if the sediment is well wetted by the continuous phase, with negligible contact between solid and gas, capillary invasion will be energetically unfavorable.³⁴

- *Cavity expansion* occurs when the bubble cannot invade adjacent pore space by capillary invasion and so the bubble creates space within the capillary network by expanding its host cavity; this mechanism is characterized by more spherical bubble geometries.¹³ Wheeler⁵ proposed that during viscoelastic displacement the soft sediment behaves as one continuous phase. Cavity expansion theory states that the greater the mechanical strength of the soft sediment, characterized according to its shear yield stress, τ , and shear modulus, G , the greater the resistance to expansion of the host pore.^{3,9}

- Many natural marine sediments^{2,37} and waste in longstanding nuclear legacy facilities^{15,41,42} are characterized by fine grain sizes and many have consolidated to high yield stresses ($\tau < 1$ kPa) over several decades^{9,16} and thus present considerable resistance to the above two mechanisms. Under these conditions the excess bubble pressure may rise until it exceeds the combined compressive and tensile strengths of the sediment, forming cracks along the direction of minimum compressive stress³⁴ by a process of *tensile fracture*.^{34,43} Jain and Juanes⁴ proposed that the excess bubble pressure for fracture scales with the inverse square of the grain size, implying that fracture will be energetically favorable in comparison to capillary invasion in very fine grained sediments. Additionally, very high strength sediments are required to support these open fractures under substantial lithostatic and hydrostatic loads.⁹

The mechanisms for bubble release are coupled to those that govern bubble growth. Under conditions that favor tensile fracture, diffusion of volatiles towards cracks promotes gas transport through the bed. Merging of these cracks with each other and with drainage channels near the bed surface can lead to the formation of stable open channels⁹ which provide a pathway for continuous gas release from the bed. High yield stress soft sediments can support stable open channels to a greater depth than weaker beds and so this represents a dominant mode of gas release in sediments with shear yield stresses greater than approximately 1 kPa.^{9,44} In weaker sediments, conducive to bubble growth by viscoelastic cavity expansion, the excess bubble pressure is able to overcome the mechanical strength of the local sediment matrix. Similarly, a bubble of sufficient buoyant force could also overcome the local bed stress restraining the bubble and *fluidize* the sediment.^{9,34} The buoyant force of the bubble increases in proportion with bubble volume, allowing larger bubbles to escape low yield stress sediments. The rise of individual bubbles by fluidization can facilitate further bubble release through *bubble cascades*,⁴⁴ where proximate bubbles are liberated in the path or wake of the rising bubble.

The potential for sudden release of large gas volumes is a critical consideration in the management of corroded nuclear wastes. Brucite, $\text{Mg}(\text{OH})_2$, is the primary precipitation product from Magnox fuel canister corrosion and has consolidated in a number of nuclear sites over several decades to form a legacy of corroded Magnox sludge (CMS), for instance within storage silos and ponds at Sellafield, UK.^{15,41} Much of the hydrogen generated within this CMS is continuously released at an acceptable rate, which is safely ventilated from tanks and silos.¹⁶ However, the accumulation of large void fractions of hydrogen within these consolidated beds over long periods has implications for the decommissioning safety case as large periodic releases could raise the concentration in any tank ullage above the lower flammability limit, facilitating the escape of radionuclides in the unlikely event of them being ignited.^{12,45} These episodic releases can occur when *waste swell* from gas retention reduces the bulk bed density below that of the convective supernatant, with this density inversion resulting in undesirable Rayleigh-Taylor instabilities.^{40,45} These *rollover events* have been implied from periodic and significant upward transfers of decay heat from the base of underground nuclear storage tanks at Hanford in the USA, which coincide with spikes in hydrogen concentration in the tank ullage.⁴⁵ Continuous gas release by fluidization and stable channel formation in weak ($\tau < 100$ Pa) and strong ($\tau < 1$ kPa) sediments, respectively, implies that intermediate strength sediments are susceptible to the most significant bed swell^{9,44} and would, therefore, present the greatest risk of episodic buoyant releases or rollover events.

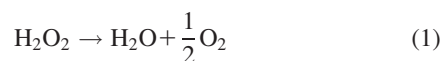
This research imitates *in situ* gas generation in waste tanks at Sellafield using the decomposition of hydrogen peroxide to form oxygen bubbles within magnesium hydroxide soft sediments over an 8–16 h period. During the experiments, the gas generation, retention, and release rates from soft sediments were monitored for a range of solids concentrations. Previous studies of bubbles within soft sediments, often using a linear elastic fracture mechanics (LEFM)^{1,38} model, have largely focused on highly consolidated beds of substantial fracture toughness,^{37–39} which are unlikely to coincide with conditions which support the largest void fractions.⁹ Here, a broad range of sediment concentrations, ranging from weak slurries close to the gel point to highly consolidated beds understood to exhibit yield stresses in the order of 1 kPa,⁴⁶ are investigated to replicate the diverse waste conditions anticipated within Magnox waste tanks. This experimental approach is combined with medical x-ray CT imaging and three-dimensional statistical analysis to reveal the nature of bubble populations retained within 30, 40, 45, and 54% w/w magnesium hydroxide soft sediments.

Materials and Methods

Test materials

The brucite test material used in this study is H3 Versamag (Martin Marietta Magnesia Specialties LLC, USA), a fine white precipitated powder with less than 1.2% oxide impurities.⁴⁷ The advertised median particle size is 1.09 μm ,⁴⁷ however, a light scattering particle size distribution using a Malvern Mastersizer revealed a median diameter of 4.4 μm , reflecting the low zeta potential of aqueous magnesium hydroxide suspensions and a tendency for rapid aggregation.⁴⁸ Soft sediments were prepared by the addition of tap water and agitation for 30 min using an overhead stirrer with an axial flow impeller. *In situ* gas generation was achieved by addition of 35% w/w hydrogen peroxide (Merck Chemicals, Germany)

which decomposes within the bed to form oxygen bubbles according to Eq. 1



It is generally accepted that the composition of the gas plays a limited role in the bubbles' buoyancy and the physics governing gas retention and release,³⁴ and so it was assumed that oxygen bubbles provide an acceptable analogue for hydrogen, while also benefiting from more controllable reaction kinetics. However, the marginally greater solubility of oxygen in water may facilitate more rapid bubble coarsening due to Ostwald ripening. A 4.4 mL volume of hydrogen peroxide was added for each liter of sediment, decomposing to a gas volume corresponding to 60% of the initial bed volume, consistent with the methodology outlined by Gauglitz et al.⁴⁴

Soft sediment rheology

The mechanical strength of soft sediments was characterized according to their shear yield stress, which was determined using two alternative vane method approaches.⁴⁹ First, a Brookfield DV-11+ Pro viscometer (Brookfield AMETEK, USA) was used to rotate four blade vanes of either 6.3 or 10 mm diameter at 0.5 rpm within the sediment to observe the measured torque, T , response over time. The vanes were submerged such that the top of the vane aligned with the surface of the sample and so the sheared surface area contained only the bottom face and the walls of an effective cylinder. Torque-time correlations were obtained in the concentration range of 30–52% w/w and the shear yield stress was determined from the maximum torque response and the vane dimensions according to Eq. 2

$$T_{\max} = \frac{\pi D^3}{2} \left(\frac{H}{D} + \frac{1}{6} \right) \tau \quad (2)$$

where H and D are the height and diameter of the vane, respectively. These results were further validated using a Bohlin Gemini rheometer (Malvern Instruments Ltd., UK), which benefits from greater measurement sensitivity and coolant flow around the sample cup for temperature regulation. A four-blade vane of 24 mm diameter was inserted into the sample for 60 s of preshear before allowing a further 60 s for the bed to recover. The shear stress was then ramped at logarithmic intervals over a broad range to observe the stress at which the instantaneous viscosity exhibits a sharp decrease by orders of magnitude, coinciding with a rapid increase in strain, thus, indicating the yield stress of the sample.⁵⁰

A series of creep tests were also conducted using the Bohlin Gemini vane-cup geometry to investigate any viscoelastic response of the sediment to fixed stress conditions.^{30,51} Following 60 s of preshear marginally above the yield point and 120 s of recovery time, to remove hysteresis effects from transferring the sample and submerging the vane, a 37.5% w/w $\text{Mg}(\text{OH})_2$ soft sediment was subjected to creep stresses in the range of 20–34 Pa for 1000 s. Deformation of the sample was observed through the increase in strain, $\gamma(t)$, obtained from the product of the instantaneous compliance, $J(t)$, and the applied stress, τ_{creep} .²⁹

$$\gamma(t) = J(t) \tau_{\text{creep}} \quad (3)$$

Laboratory scale gas retention tests

A series of laboratory scale tests were conducted to investigate the capacity for gas retention under different bed yield

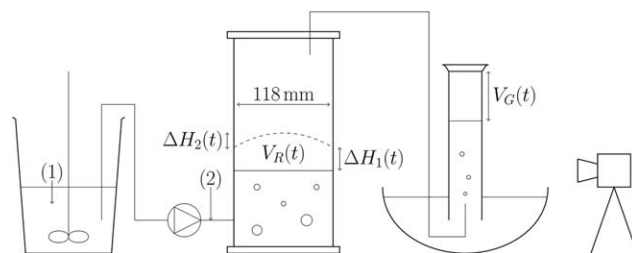


Figure 1. Schematic of the laboratory scale gas retention tests identifying two alternative hydrogen peroxide injection points, 1 and 2; the dashed line represents the surface of the soft sediment at time t .

stress conditions. A 1 L volume of soft sediment was pumped to a 118 mm diameter acrylic test cylinder using a peristaltic pump. Hydrogen peroxide was injected into the soft sediment either at the mixing stage (Stage 1) or by slow continuous injection during the 2 min transfer period (Stage 2) as demonstrated in Figure 1. Optical images of the test vessel were captured at 8 min intervals while the hydrogen peroxide decomposed to form oxygen bubbles causing the bed to expand. The generated gas volume, $V_G(t)$, was monitored over time by measuring the volume of water displaced from an adjacent upturned measuring cylinder in a water bath. The retained gas volume, $V_R(t)$, was determined from the net increase in bed volume during gas generation. The sediment height, both at the cylinder wall and at the center of the test vessel, was measured to millimeter precision from the images of the bed, referencing the measuring scale on the test cylinder wall for calibration. The instantaneous bed volume was estimated by representing the bed as a cylinder with a spherical cap according to Eq. 4

$$V_R(t) = \pi R^2 \Delta H_1(t) + \frac{1}{3} \pi \Delta H_2(t)^2 (3R - \Delta H_2(t)) \quad (4)$$

where R is the test cylinder radius, $\Delta H_1(t)$ is the increase in bed height at the wall and $\Delta H_2(t)$ is the difference in height between the domed sediment peak and the bed height at the wall (see Figure 1). The bed void fraction, $v(t)$, can be calculated at any instant using Eq. 5

$$v(t) = \frac{V_R(t)}{V(t)} \quad (5)$$

where $V(t)$ is the instantaneous bed volume.

The capacity of each soft sediment to retain gas is characterized according to the maximum void fraction, v_{\max} , observed during the experiments. As the gas generation profiles were designed for consistency between tests, bed expansion is governed by the rate of gas release. The instantaneous volume of gas which has escaped the bed, $V_E(t)$, is implied from the difference between the generated and retained volumes

$$V_G(t) = V_R(t) + V_E(t) \quad (6)$$

The density, ρ , of a magnesium hydroxide soft sediment of known solids weight fraction, ω , and void fraction, v , can be determined using Eq. 7

$$\rho(\omega, v) = (1-v) \rho_s = \frac{1-v}{\left(\frac{\omega}{\rho_p} + \frac{1-\omega}{\rho_f} \right)} \quad (7)$$

where ρ_s is the gas free bulk soft sediment density, ρ_p is the particle density and ρ_f is the fluid density. Hence, it is possible

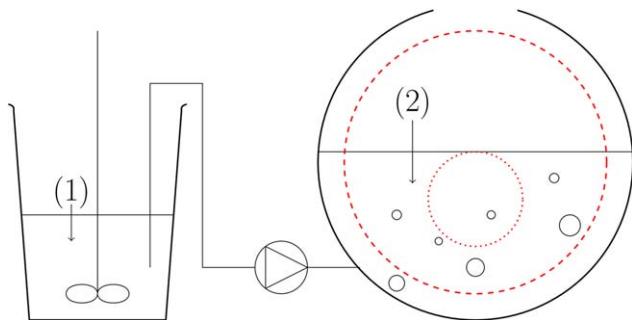


Figure 2. Schematic of the modified gas retention tests for optimized CT imaging, identifying two alternative hydrogen peroxide injection points, 1 and 2, and two alternative imaging fields of view in red.

[Color figure can be viewed at wileyonlinelibrary.com]

to determine the void fraction at which the soft sediment bulk density would become buoyant with respect to an aqueous supernatant and rollover events become feasible.

X-ray computed tomography

The laboratory scale gas retention tests provide a good indication of bulk bed swell under different sediment conditions but reveal little about the bubble population retained within the optically opaque bed. A Brivo CT385 medical x-ray computed tomography (CT) scanner (GE Healthcare, UK) was used to provide insight into the size, shape, and number density of the retained bubble population within soft sediments of 30, 40, 45, and 54% w/w solids concentration, reflecting the broad range of density and yield stress conditions anticipated within Magnox waste tanks.⁴⁶ The test vessel geometry was replaced with a sideways mounted cylinder of 30 cm diameter and 15 cm length to ensure that x-ray attenuation through the sample was as axisymmetric as possible, thereby minimizing artefacts. Sediment preparation was scaled up from 1 to 6.5 L to utilize the greater test vessel capacity. The effect of nonhomogeneous gas generation through the test material was investigated by injecting hydrogen peroxide into the soft sediment during transfer to the test vessel (Stage 2), as represented in Figure 2.

Figure 2 also demonstrates the two imaging fields of view (FOV) investigated. The small FOV captures a volume 49 times smaller than the large FOV, but achieves almost double the pixel resolution and half the axial slice separation, as detailed in Table 1. The small FOV was captured more frequently and so was primarily used to examine transient changes in the bubble population. The large FOV was used to ensure representative statistics of the entire vessel and observe the larger macrofeatures propagating through the bed. The pixel resolution of the large FOV is an order of magnitude

Table 1. X-ray CT Imaging Parameters for Two Imaging Fields of View

	Large FOV	Small FOV
X-ray voltage (kV _p)	120	120
X-ray tube current (mA)	40	79
FOV diameter (mm)	250	96
Pixel resolution (μm)	488	250
Slice separation (μm)	1250	625
Number of axial slices	112	32
Axial FOV depth (mm)	138.8	19.4
Total FOV volume (mm ³)	6.81 × 10 ⁶	1.40 × 10 ⁵

larger than the median sediment grain size, so only mature bubbles significantly larger than the scale of capillaries within the sediment were observed.

X-ray CT image analysis. The statistics of the retained bubble population were determined by three-dimensional analysis using FIJI-ImageJ software.³⁵ A stack of CT images was first thresholded to create binary images of black bubbles against white soft sediment. Discrete bubbles were then identified by interconnecting the black voxels which were face, edge, or corner adjacent using the 3-D object counter algorithm provided by Bolte and Cordelières.⁵² The volume, V , surface area, A , and co-ordinates of each individual bubble were then recorded for further analysis using Matlab (Mathworks, v. R2013b). The bubble size is represented in this study using the equivalent spherical diameter, $d_b = \sqrt[3]{\frac{6V}{\pi}}$, while the bubble shape was analyzed using a digital sphericity, Ψ_{dig} , defined in Eq. 8. Traditional sphericity calculations performed on bubbles comprised of regular cuboid voxels will be artificially low as the angular voxels exaggerate the surface area of the bubble. As the sphericity of even a perfect digital sphere cannot exceed the sphericity of a cube ($\Psi_{\text{cube}} = (\frac{2}{6})^{\frac{1}{3}} \approx 0.806$), the digital sphericity normalizes the conventional sphericity against that of a cube to provide ceiling values closer to unity.

$$\Psi_{\text{dig}} = \frac{\pi^{\frac{1}{3}}(6V)^{2/3}}{A} \left(\frac{6}{\pi}\right)^{\frac{1}{3}} = \frac{6}{A} V^{\frac{2}{3}} \quad (8)$$

As thresholding represents the critical stage of image postprocessing, sensitivity analysis was undertaken to investigate the impact of the chosen threshold value on the ultimate bubble statistics. Using the example of the 40% w/w soft sediment, the Renyi entropy algorithm⁵³ was applied to calculate a threshold radiodensity of -315 HU, and a range of ±38 HU around this value was investigated, as shown in Figure 3. The range of threshold values had a negligible impact on the resulting bubble diameter histogram, with standard deviations of 2.5

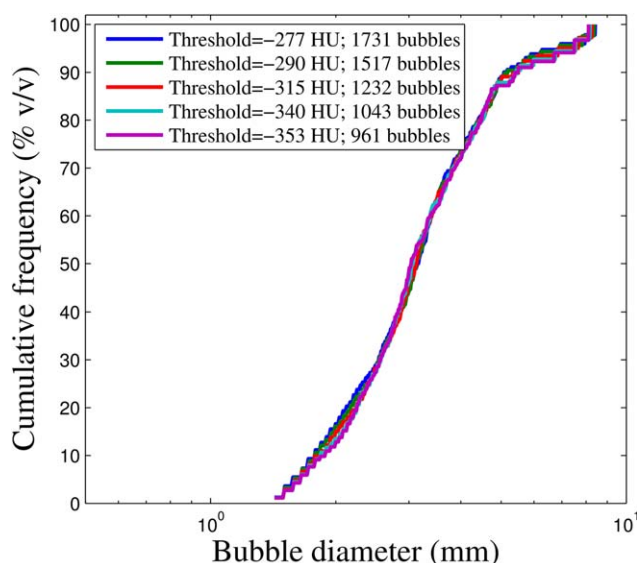


Figure 3. Sensitivity of bubble population statistics to the threshold radiodensity value used during image postprocessing; the statistics relate to bubbles within the large FOV of a 40% w/w sediment after 6 h of gas generation.

[Color figure can be viewed at wileyonlinelibrary.com]

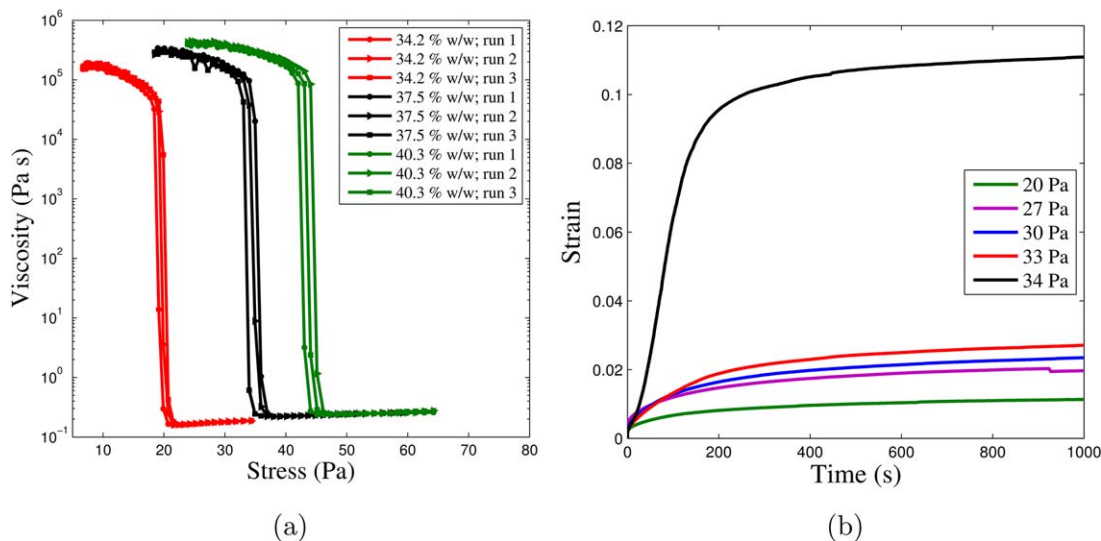


Figure 4. The flow behavior of magnesium hydroxide soft sediments demonstrated by (a) the instantaneous viscosity evolution in response to a shear stress ramp for 34.2–40.3% w/w sediments and (b) creep profiles at a series of constant stress conditions for a 37.5% w/w sediment.

[Color figure can be viewed at wileyonlinelibrary.com]

and 4.2% observed in the 50th, $d_{b,50}$, and 90th, $d_{b,90}$, percentiles of the equivalent spherical bubble size distributions, respectively. However, while the bubble size distribution within this observable size range was not particularly sensitive to thresholding, the number of mature bubbles consisting of more than 5 voxels within the FOV varied significantly between 961 and 1731 (shown in the legend of Figure 3). This discrepancy reflects the large number of small bubbles close to the pixel resolution, and the fact that small bubbles contain a large number of surface voxels with intermediate radiodensities between those of the bulk sediment and oxygen. Nonetheless, the influence of the thresholding value on the exact measurement of the bubble number density was not considered significant, as the study's focus was on the transient trends in the number, size, and shape of mature bubbles within the population, which were less sensitive to the given threshold value.

Transient changes in the bubble population were examined using a process of *hyperstacking*. Collating multiple stacks of two-dimensional tomographs at known time intervals into a hyperstack enables panning along the depth of the FOV and through time. By *flattening* the hyperstack, different time frames can be represented using a color progression, enabling visualization of changes in the number, size, shape, and position of bubbles within the FOV.

Results and Discussion

Soft sediment rheology and shear yield stress characterization

Stress controlled flow curves for $\text{Mg}(\text{OH})_2$ soft sediments at three solids concentrations are presented in Figure 4a. The nine flow curves demonstrate the same characteristic behavior, with a high viscosity plateau at low shear stresses, a yield stress, indicated by the six orders of magnitude decrease in viscosity over a very narrow stress range, and a secondary low viscosity plateau above the yield point. The rapid fall in viscosity at the yield point is accompanied by an equally rapid increase in strain, as the vane readily deforms the sediment on transition to more fluid-like behavior.⁵⁴ The yield stress at

each solids concentration demonstrates good repeatability between samples and increases with solids concentration.

This apparently elastic or solid-like response at low stress and viscous, fluid-like, response above the yield stress is consistent with viscoplastic behavior.^{55,56} However, the four creep profiles in Figure 4b performed using an imposed stress below the yield stress, $20 \leq \tau_{\text{creep}} \leq 33$ Pa, suggest this interpretation does not fully capture the complex sediment rheology. The continued linear rise in strain apparent after 400 s, once the contribution of the instantaneous and delayed elastic compliances have diminished, demonstrates distinctly viscous behavior below the yield point. At the lowest stress, $\tau_{\text{creep}} = 20$ Pa, the viscous compliance is especially significant in comparison to the delayed elastic response. The departure from this type of creep behavior in the 34 Pa test, with much more extensive deformation of the sample during the first 100 s, indicates the transition to more fluid-like behavior,^{29,51,56} indicating a yield stress in the 33–34 Pa range, which is consistent with the 37.5% w/w flow curves in Figure 4a.

A summary of the shear yield stress characterization for magnesium hydroxide soft sediments, using both the Brookfield viscometer and the Bohlin rheometer data, is presented in Figure 5. The smaller Brookfield vane (vane 73) was required for samples above 40% w/w concentration to operate within the maximum torque limits of the viscometer, but resulted in greater scatter in the measured yield stress. This is influenced by a number of factors: the uncertainty in the yield stress measurements increases as the area of the sheared surface is reduced, samples with higher solids content are more difficult to homogeneously mix, and these increased uncertainties coincide with a region of sharp yield stress increase with solids concentration. Nonetheless, the collated data from all three vanes generated a power law fit with concentration, shown in Eq. 9, with a robust coefficient of determination of $R^2 = 0.96$

$$\tau = 2.156 \times 10^5 \omega^{8.55} \quad (9)$$

This relationship was used to characterize the yield stress of samples used in subsequent laboratory scale gas retention tests and x-ray CT imaging.

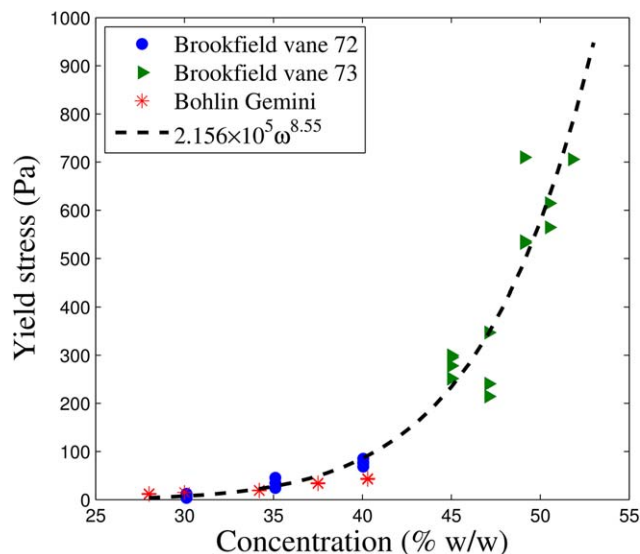


Figure 5. The shear yield stress of magnesium hydroxide soft sediments obtained using the vane method.

[Color figure can be viewed at wileyonlinelibrary.com]

Laboratory scale gas retention tests

Injecting hydrogen peroxide into 28–45% w/w magnesium hydroxide soft sediments at stage 2 in Figure 1 resulted in the gas generation profiles shown in Figure 6a. Increasing solids concentration in the bed demonstrated no enhanced catalytic effect on the rate of hydrogen peroxide decomposition. Good repeatability was achieved between the four gas generation profiles in Figure 6a and complete conversion of 4 mL hydrogen peroxide generated 548 ± 62 mL oxygen in 14–18 h. The total volume of oxygen generated was in line with expectations as 4 mL of 35% w/w hydrogen peroxide solution contains 4.65×10^{-2} mol H_2O_2 , decomposing to 2.33×10^{-2} mol O_2 , which would occupy a 568 mL volume in the gas phase at 25°C and 1 atm. The rate of gas generation exponentially

decays as the hydrogen peroxide is consumed, observed as a pseudo first-order reaction in the form of Eq. 10

$$V_G(t) = V_{G,f}(1 - \exp(-kt)) \quad (10)$$

where $V_{G,f}$ is the final volume of gas generated and k is a first-order reaction kinetic constant in the order of 0.17 – 0.3 h^{-1} for these laboratory scale tests. Two dashed line profiles in Figure 6a represent example fits in accordance with Eq. 10. The rate of oxygen production was sensitive to local temperature conditions and so subsequent tests conducted within a CT scanner exhibited accelerated hydrogen peroxide decomposition, approaching completion within 8 h due to the heat generated by operating the scanner, corresponding to kinetic constants closer to 0.4 h^{-1} . The variation in total generated gas volume can be attributed to fluctuations in ambient temperature and the precision of the syringe used to inject the hydrogen peroxide; as 1 mL 35% w/w hydrogen peroxide decomposed to around 137 mL oxygen, the total gas volume was sensitive to the precise volume of gas generating reagent introduced. Nonetheless, these gas generation profiles demonstrate sufficient repeatability across the relevant bed concentration range.

Figure 6b demonstrates gas generation, retention, and implied release profiles observed during 15 h of *in situ* gas generation in a 35% w/w magnesium hydroxide soft sediment of 27 Pa shear yield stress. During the first 4 h around two thirds of the gas generated is retained by the bed, after which the rate of bed expansion decreased, with the bed attaining a maximum void fraction of 0.27. At 27% voidage, the bulk density of the bed is reduced to 10% below that of water, indicating a significant possibility of rollover events in the presence of a supernatant. The absence of a supernatant for these tests precluded large episodic releases due to Rayleigh-Taylor instabilities, and gas appeared to be continuously released from the bed at a near constant rate of 21 mL h^{-1} (red line, Figure 6b), with just over half of the total gas generated escaping the bed over the course of the 15 h experiment. This methodology was repeated for bed concentrations of 28–54% w/w, corresponding to varied yield stress conditions in the range of 4–1112 Pa. The gas retention and release profiles obeyed

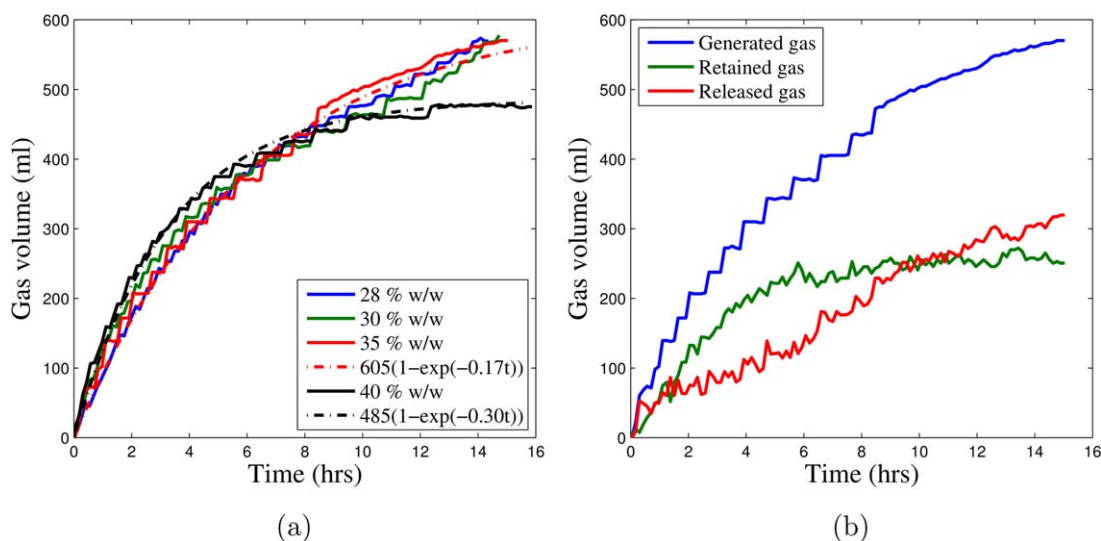


Figure 6. Laboratory scale gas retention test profiles achieved by injecting hydrogen peroxide at point 2 in Figure 1, including (a) example gas generation profiles within 28–40% w/w (4–85 Pa) soft sediments and (b) gas generation, retention and release profiles within 35% w/w (27 Pa) soft sediment.

[Color figure can be viewed at wileyonlinelibrary.com]

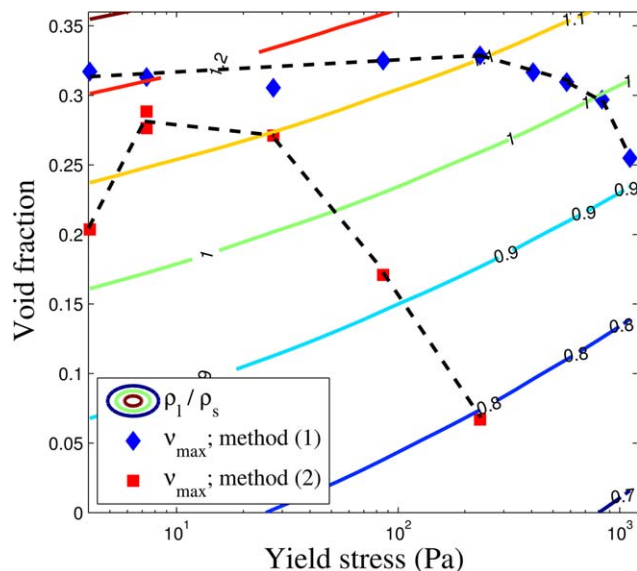


Figure 7. The maximum void fractions observed under different shear yield stress conditions and alternative gas generation methods: (1) injection at the sample homogenization stage and (2) continuous injection into the flow during transfer to the test vessel (see Figure 1); the density contour map demonstrates the feasibility of periodic rollover events.

[Color figure can be viewed at wileyonlinelibrary.com]

similar trends across the yield stress range, but the maximum void fractions varied between each soft sediment and are presented in Figure 7.

Injection of hydrogen peroxide at Stage 2 (see Figure 1) generated a parabolic trend in the maximum void fraction across the 4–234 Pa yield stress range, implying enhanced rates of continuous gas release below 7 Pa and above 27 Pa shear yield stress. Below 7 Pa yield stress, the buoyant force of even relatively small bubbles should be sufficient to fluidize the weakly consolidated, milky sediment.⁹ The fall in maximum void fractions above 27 Pa yield stress appears to relate to a more complicated phenomenon. The rate of gas release by fluidization should progressively decrease with increased bed yield stress,^{9,18} while gas release along stable open channels is more typically associated with significantly more consolidated beds with yield stresses greater than 1 kPa.⁹ Thus, neither mechanism at present would adequately explain the significantly increased rate of gas release from beds of 84–234 Pa yield stress. It was felt that a potential cause may be related to mixing inhomogeneity, with continuous peroxide injection into the feedline resulting in a nonuniform distribution of volatiles, leading to the creation of localized release pathways. Consequently, an alternative approach was investigated by introducing hydrogen peroxide at the sample homogenization stage (indicated by stage 1 in Figure 1), ensuring more thorough mixing of gas generating reagents through the soft sediment.

Homogenization of hydrogen peroxide through the sediment resulted in consistently high void fractions of 0.3–0.33 across a broad range of yield stress conditions up to 600 Pa, while the capacity for bed swell only receded in the 600–1200 Pa range. The fall in maximum void fraction in the 600–1200 Pa range coincides with bed conditions that have previously been

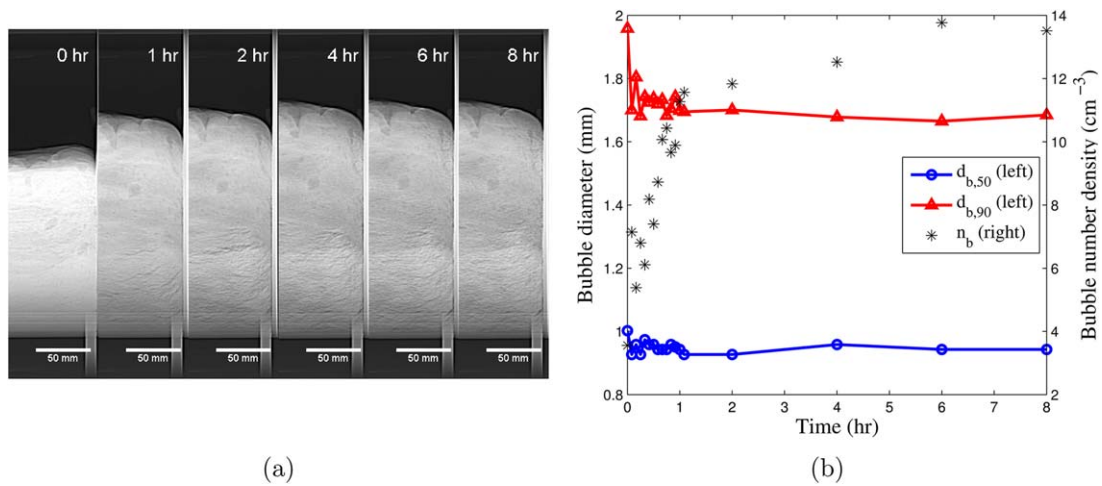
associated with the continuous release of gas along stable open channels.⁹ The reason for this disparity in bed expansion between the two approaches to peroxide introduction was uncertain, and so both experimental approaches were explored using x-ray CT imaging to identify whether differences between the retained bubble populations reveal alternative mechanisms for gas release.

Cross-referencing the experimental maximum void fractions with the density contour lines, calculated using Eq. 7, in Figure 7 reveals critical yield stress conditions where bed swell reduces the bulk sediment density to below that of water, invoking the potential for rollover events and acute gas release. Peroxide addition using method 2 resulted in a narrow range of $4 \leq \tau \leq 60$ Pa where sediments exhibit sufficient bed expansion to achieve buoyancy. Under the more homogeneous gas generation conditions assumed with injection method 1, the capacity for rollover events remains feasible for highly consolidated bed conditions of up to 800 Pa yield stress. CMS legacy waste in the Magnox Swarf Storage Silos at Sellafield has consolidated over several decades under large lithostatic loads to achieve yield stress conditions believed to be in excess of 1 kPa.^{16,42,46} These highly consolidated, highly heterogeneous bed conditions appear to facilitate sufficient continuous gas release to mitigate the risk of large periodic releases; however, evacuating aging facilities of these legacy wastes requires their mobilization, dilution, homogenization, transportation, and storage in new containers. Consequently, these processing steps would appear to make the conditions conducive to rollover events more credible, at this reduced experimental scale, and so measures should be considered to assess this risk at process scale and mitigate against large episodic releases. These measures could involve the provision of sufficient ullage capacity that the lower flammability limit can never be approached, by dewatering CMS in its new storage environment to high yield stress conditions which facilitate higher levels of continuous gas release for safe ventilation, or by using an alternative approach to shielding radiation, without using an aqueous supernatant.

X-ray Computed Tomography

Evolution in the bubble size and shape

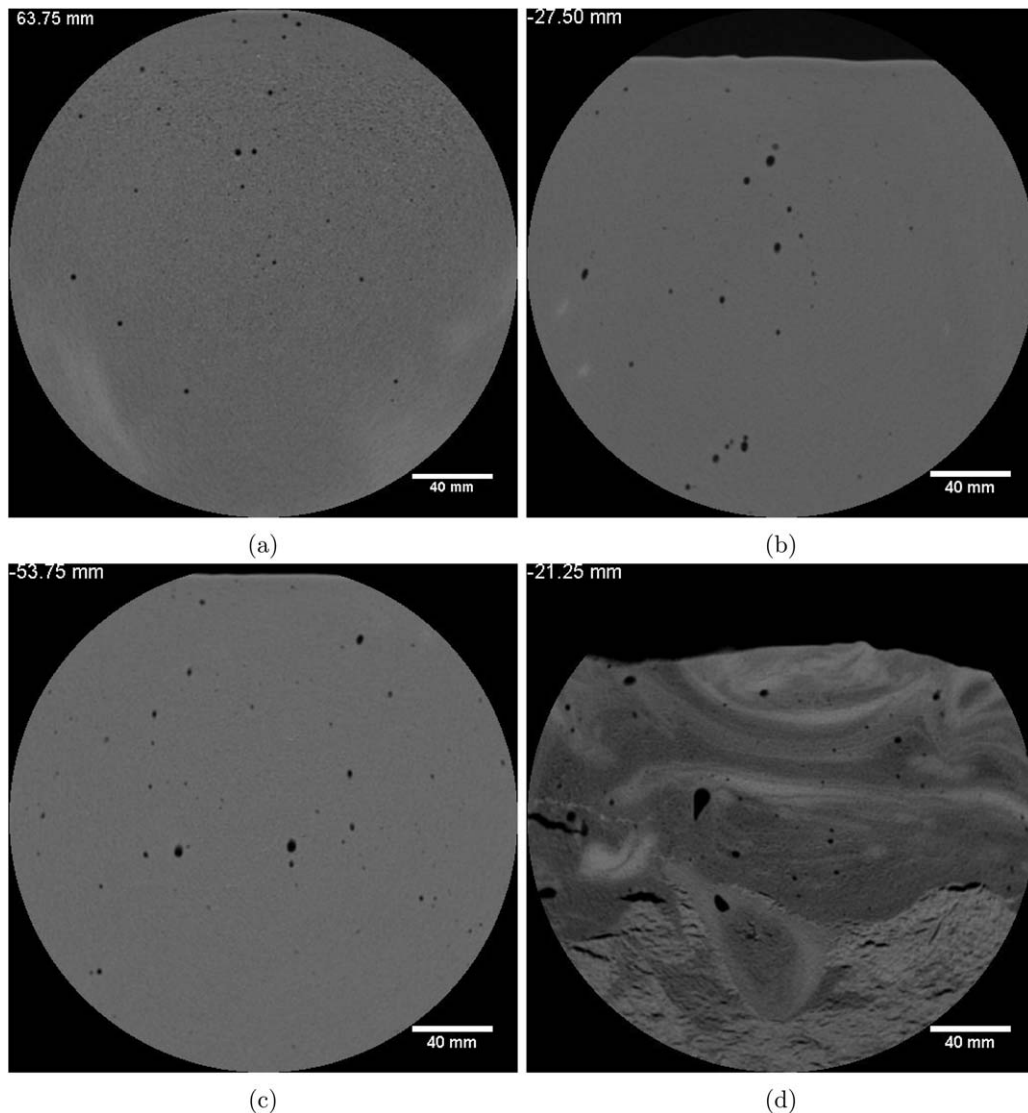
The four soft sediments of 30, 40, 45, and 54% w/w solids concentration imaged using x-ray CT correspond to yield stresses of 7, 86, 234, and 1112 Pa. Using the example of the 1112 Pa sediment, six side-on scout profiles of the bed, presented in Figure 8a, demonstrate expansion of the bed during the first 4 h of gas generation, similar to the gas retention profile in Figure 6b, with negligible bed swell thereafter. The bulk bed expansion contrasts with the evolution of the bubble population of an observable scale ($d_b \geq 0.72$ mm) within the small FOV, presented in Figure 8b. The $d_{b,50}$ and $d_{b,90}$ bubble diameters appear to achieve steady state sizes within the first hour of gas generation. Expansion of the bulk sediment in Figure 8a appears to be mirrored by the increase in the number density, n_b , of bubbles at this observable scale, presented on the right-hand axis of Figure 8b. The number density of bubbles greater than 0.72 mm equivalent spherical diameter increases rapidly within the first two hours of gas generation, slowing significantly from 2 to 6 h and remaining relatively stable thereafter. Thus, the data reveal that the population of mature, macroscopic bubbles increases during the period of greatest bed expansion, and slows as the bulk bed volume



(a) (b)

Figure 8. The evolution of retained bubble populations within 1112 Pa yield stress soft sediment including (a) side-on x-ray *scout* images of half the bed showing bulk waste swell during 0–8 h gas generation and (b) the evolution of bubble size and number density with time within the small FOV.

[Color figure can be viewed at wileyonlinelibrary.com]



(a) (b) (c) (d)

Figure 9. X-ray tomographs of bubbles within the large FOV of (a) 7 (b) 86 (c) 234, and (d) 1112 Pa yield stress magnesium hydroxide soft sediments after 6 h gas generation; the values in the top left corner of each image represent the axial distance from the center of the test vessel.

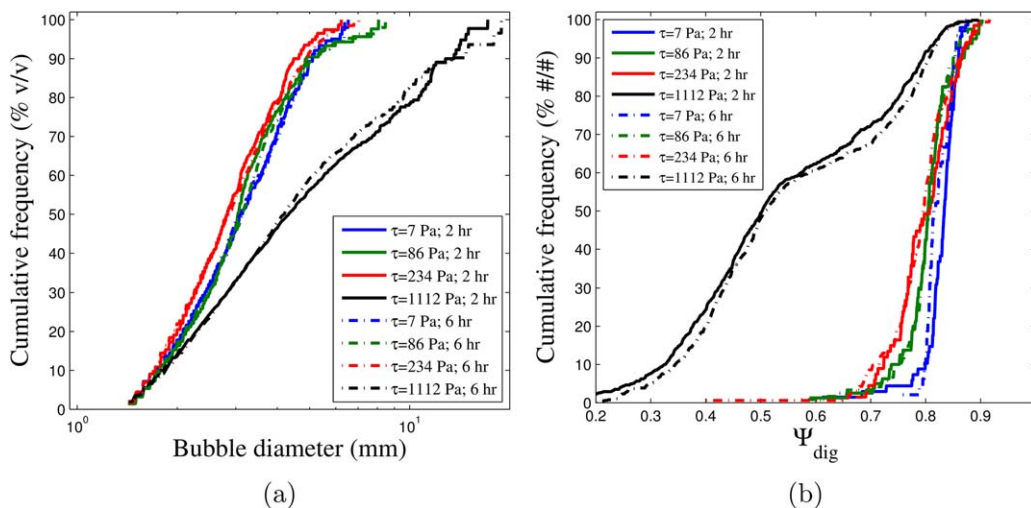


Figure 10. Histograms of (a) bubble diameter (volume weighted, bubbles < 5 voxels excluded) and (b) bubble sphericity (count weighted, bubbles < 80 voxels excluded) within 7–1112 Pa soft sediments after 2 and 6 h gas generation.

[Color figure can be viewed at wileyonlinelibrary.com]

plateaus. While this evolution in the bubble population appears to imply higher rates of bubble nucleation within the early stages of gas generation, this cannot be monitored directly, as any significant population of microbubbles is not recognized at this resolution. Indeed, if growth of subresolution bubbles to the observable scale proceeds by coalescence or by Ostwald ripening, it is possible that the number density of small bubbles could diminish as the population of mature bubbles increases. Conversely, the largest, most mature bubbles exhibit either negligible growth within this time frame, or the gas release mechanism imposes a ceiling in the maximum bubble dimension that the bed is able to support. In either instance, the observable mature bubble population can be considered to reach an equilibrium size distribution and number density, representative of the bed at maximum voidage, after 6 h of hydrogen peroxide decomposition.

This observation of a steady state bubble population within the 1112 Pa yield stress sediment after 6 h of gas generation holds equally true for sediments of 7, 86, and 234 Pa yield stress. Tomographs within the large FOV of all these magnesium hydroxide soft sediments after 6 h gas generation are presented in Figure 9, while corresponding size and shape analysis of each of the bubble populations at 2 and 6 h are presented in Figure 10. The 7, 86, and 234 Pa tomographs in Figure 9 are all characterized by relatively small, regular shaped, dispersed bubbles, the largest of which range from 6.5 to 9 mm equivalent spherical diameter. Laplace pressures, which promote spherical curvature, scale with inverse bubble diameter, and so small bubbles are anticipated to be highly spherical in nature. The largely spherical nature of mature bubbles within these 7–234 Pa sediments is consistent with a fluid-like response of the sediment to the stress of the growing bubble. However, after excluding the smaller bubbles comprised of fewer than 80 voxels ($d_b \leq 3.56$ mm), Figure 10b shows a small but distinct decrease in sphericity with increased yield stress within this range. This is explained by the fact that sediments of increased strength or greater depth typically demonstrate greater anisotropy in their stress tensors,³⁴ often reported through reductions in Poisson's ratio,^{9,14} thereby promoting less axisymmetric bubble growth. Similarly, Algar and

Boudreau³⁶ use LEFM modeling to predict an increase in bubble aspect ratios for growth within sediments of increased Young's modulus.

Figure 10a demonstrates no significant evolution in the observable bubble size distribution within any of the soft sediments between 2 and 6 h, consistent with the observations from Figure 8b. The similarity in bubble size distribution within 30–45% w/w beds, despite a 33-fold increase in the shear yield stress of the surrounding sediment, seems to conflict with our current understanding of bubble retention in low and intermediate strength beds.^{9,44} Bubble fluidization, possibly inducing bubble cascades, is thought to be the main mechanism by which dispersed bubbles are released from these relatively low strength beds.⁹ A bubble's buoyant force, $F_b = \frac{\pi}{6} d_b^3 (\rho_s - \rho_g) g$, increases in proportion to its volume while the restraining force of the surrounding bed, $F_r \propto \tau d_b^2$, can be characterized by the product of its shear yield stress and the bubble cross sectional area. The ratio of these volume- and area-dependent competing forces, therefore, determines a critical bubble diameter, $d_{b,crit}$, to which a bubble must grow for the buoyant force to become dominant enabling the bubble to fluidize the local bed. This critical bubble diameter is often estimated using Eq. 11^{9,18}

$$d_{b,crit} = Y \frac{\tau}{(\rho_s - \rho_g) g} \quad (11)$$

where Y is a material dependent dimensionless *yield parameter* reported in the range of 0.023–0.061¹⁸. The relationship in Eq. 11 implies that the size of bubble which a bed is able to support increases in proportion to the ratio of a bed's yield stress to its bulk density. Increasing the solids concentration of the bed from 30 to 45% w/w sees this ratio increase by a factor of 28, however, this does not manifest in any observable increase in the size distributions of the mature bubble populations within these 7–234 Pa yield stress sediments.

Two theories could explain why the population appears to achieve a steady state size distribution, long before gas production is exhausted, that is seemingly independent of sediment strength within the 7–234 Pa yield stress range. First, the

high sphericity of bubbles within these sediments implies a fluid-like response to the stress of the growing bubble. As such, the rate of bubble growth may be limited by diffusion rather than by the elastic resistance of the sediment during bubble growth. Under these circumstances Boudreau et al.⁵⁷ model the instantaneous bubble diameter using the expression in Eq. 12

$$d_b^2(t) = \frac{4\phi D_{\text{eff}}}{c_g} \left(\frac{S(t)R_1^2}{3D_{\text{eff}}} + c_1 - \frac{c_g}{K_h} \right) t + d_{b,0}^2 \quad (12)$$

where, in this instance, the rate of oxygen generation within the pore water, $S(t)$, or source term, is time dependent, as evidenced by the gas generation profiles in Figure 6a. The remaining terms include the sediment porosity, ϕ , the effective diffusion coefficient for oxygen through the sediment, D_{eff} , which should account for the tortuosity of the diffusion path through the sediment matrix, the oxygen concentrations within the bubble, c_g , and within the pore water, c_1 , at a radius of R_1 , the dimensionless Henry's law coefficient, K_h and the initial bubble diameter, $d_{b,0}$. Given the oxygen generation profiles in Figure 6a, it is clear that the source term exponentially diminishes with time, $S(t) = S_0 \exp(-kt)$, where S_0 is the initial source strength. This implies that the bubbles which are nucleated later in the experiment will grow to a smaller ultimate diameter, which could partially explain the plateau in bubble diameter. However, the impact of the exponentially diminishing oxygen source becomes clearer when differentiating Eq. 12 to generate the expression for bubble growth rate in Eq. 13

$$\begin{aligned} \frac{d}{dt} d_b^2(t) &= \frac{4\phi D_{\text{eff}}}{c_g} \left(\frac{R_1^2}{3D_{\text{eff}}} \left(S(t) + \frac{dS(t)}{dt} t \right) + c_1 - \frac{c_g}{K_h} \right) \\ &= \frac{4\phi D_{\text{eff}}}{c_g} \left(\frac{R_1^2 S_0}{3D_{\text{eff}}} (1-kt) \exp(-kt) + c_1 - \frac{c_g}{K_h} \right) \end{aligned} \quad (13)$$

This expression includes a source strength term, $\left(S(t) + \frac{dS(t)}{dt} t \right)$ and a concentration gradient term which drives diffusion towards the bubble, $\left(c_1 - \frac{c_g}{K_h} \right)$. The source strength term will rapidly diminish with time due to the exponential component, becoming negative at $t > k^{-1}$ and reaching a minimum at $t = 2k^{-1}$. Thus, for a kinetic constant of 0.4 h^{-1} , as observed during the CT experiments, Eq. 13 predicts that mature bubbles could cease to grow at some time between 2.5 and 5 h, depending on the magnitude of the concentration gradient within the pore water, despite continued oxygen production for 8 h of experimentation.

Under these circumstances the sediment's capacity to resist stress is entirely neglected, however Algar and Boudreau³⁶ describe another mechanism whereby elastic materials, which can support stress, may achieve a *no growth* condition, as previously observed in Gardiner et al.³⁸ Resistance to bubble growth due to the mechanical strength of the sediment enables the internal pressure of the bubble to rise above ambient pressure, in contrast to growth within conventional viscous fluids which cannot support stress.³⁶ This causes the concentration of oxygen within the bubble to rise, thus causing the concentration gradient which drives diffusion toward the bubble to diminish. For very low source strength or weak supersaturation conditions, a relatively small increase in concentration within the bubble could eliminate the concentration gradient and starve the bubble of oxygen for continued growth. The initial source strength can be characterized from the initial bulk

concentration of hydrogen peroxide in the pore water, $c_{\text{H}_2\text{O}_2}$, the stoichiometric ratio of oxygen, $\nu_{\text{O}_2} = 0.5$, and the kinetic constant as follows

$$\int_0^\infty S_0 \exp(-kt) dt = \frac{S_0}{k} = \nu_{\text{O}_2} c_{\text{H}_2\text{O}_2} \quad (14)$$

Using the example of the 86 Pa sediment in Figure 9b, which had an initial hydrogen peroxide concentration of $5.9 \times 10^{-2} \text{ M}$ and an observed kinetic constant in the order of 0.4 h^{-1} , the initial source strength would be $3.29 \times 10^{-6} \text{ M s}^{-1}$. Hence, the initial source strength is relatively strong,³⁶ although it will diminish by an order of magnitude every 6 h. The *no growth* condition is more likely attained due to the weak supersaturation of oxygen within the porewater. Every mole of oxygen generated by reaction would saturate the pore water in the bed at a maximum concentration, $c_{\text{O}_2}(\text{aq})$, of $2.99 \times 10^{-2} \text{ M}$. This concentration is less than a quarter of the critical concentration for homogeneous oxygen nucleation in pure water, c_{nuc} , which is reported at 0.12 M ,⁵⁸ implying that free gas bubbles form by heterogeneous nucleation at a relatively weak supersaturation. Consequently, the rapidly diminishing oxygen source strength which limits diffusion controlled growth and the mild increase in internal bubble pressure required to extinguish the oxygen concentration gradient under these apparently weak supersaturation conditions are both likely to contribute to the cessation of mature bubble growth long before oxygen production is fully exhausted.

The similar bubble size distributions within 7–234 Pa sediment in Figure 10a contrast with the 1112 Pa yield stress bed, which retains much larger bubbles of up to 20 mm equivalent spherical diameter. The largest voids exhibit two distinct geometries in Figure 9d; some distorted ellipse and inverted teardrop geometries coexist alongside lateral cracks which are more prevalent within deeper regions of the bed and within brighter regions of sediment (indicative of an elevated solid concentration). This heterogeneity in gray-scale within the bulk sediment, away from the bubbles, in Figure 9d demonstrates the difficulties experienced when homogenizing magnesium hydroxide soft sediments with solids concentrations in excess of 50% w/w. The two distinct void geometries are captured by the bimodal sphericity histogram for bubbles within the 1112 Pa sediment in Figure 10b, and are consistent with the cavity expansion and tensile fracture mechanisms for bubble growth. The lowest digital sphericities in Figure 10b correspond to fracture sites with the largest aspect ratios. These cracks propagate laterally as the compressive bed stress is lowest normal to the direction of the lithostatic load. Many of the fracture sites imaged within the large FOV of the 1112 Pa material extended to the walls of the test vessel, and so gas diffusion toward these cracks presents a route for continuous gas release from the sediment. The inverted teardrop shapes are consistent with bubbles observed by Katsman,³⁹ Algar et al.,³⁷ Takada,³² and Weertman,³¹ who investigated bubbles in a range of viscoelastic materials including marine sediment, gelatin and magma, and are explained by the surrounding pressure field in the soft sediment increasing linearly with depth. As the bubble grows, the pressure difference across the height of the bubble increases, the pressure at the bubble *tail* diminishes and the teardrop geometry emerges as the tail pressure falls to near zero.³⁷ The increase in pressure field with depth also promotes faster growth at the shallow surface of the bubble.³⁷

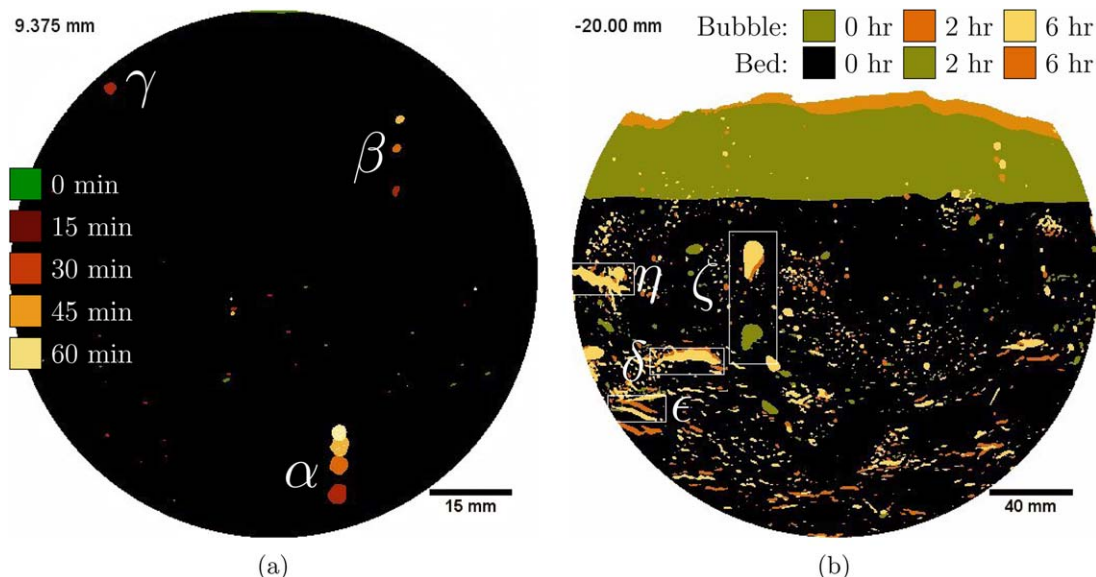


Figure 11. Hyperstacked x-ray tomographs of bubbles in 7 and 1112 Pa soft sediments using a color legend to represent bubbles across multiple time-frames, showing (a) bubbles at 15 min intervals within the small FOV of a 7 Pa soft sediment and (b) bubbles at 0, 2, and 6 h within the large FOV of a 1112 Pa soft sediment (as the sediment expands due to its increasing voidage the bulk sediment changes from black to green to orange as shown in the legend).

[Color figure can be viewed at wileyonlinelibrary.com]

Bubble mobility, residence times and release

Figure 6b revealed that gas is continuously released from a 27 Pa sediment at a near constant rate of around 21 mL h^{-1} . The slowest gas release was observed when hydrogen peroxide was introduced to sediments of 4–234 Pa at the sample homogenization stage, corresponding to rates of around 17 mL h^{-1} . This continuous gas release must be reconciled with the observations that the size distribution of the mature bubble population remains constant and independent of yield stress in the 7–234 Pa range, and that there are no major disturbances in the topography or profile of the bed from either the tomographic images of the bed, as shown in Figure 8a, or from continuous digital photography of the sediment. Transient x-ray CT was used to investigate whether the mobility of bubbles within the sediment correlate to the observed rates of gas release.

Figure 11 presents tomography of the 7 and 1112 Pa beds across multiple time frames using hyperstacking. Figure 11a shows bubbles at 15 min intervals within a 7 Pa magnesium hydroxide soft sediment. The vast majority of small bubbles visible at 0 or 15 min appear only once within this slice through the sediment, indicating residence times within this 96-mm diameter FOV of less than 15 min. This could suggest that many bubbles grow very quickly to buoyant dimensions ($d_b > d_{b,crit}$) and escape the low strength sediment matrix by fluidization. In support of this theory, the bubble labeled “ γ ” is only captured within the 30-min scan, suggesting that this bubble grew from subpixel dimensions ($d_b \leq 250 \text{ mm}$) to 2.2 mm diameter in less than 15 min, demonstrating that rapid bubble growth is realistic. The two other labeled bubbles, “ α ” and “ β ,” exhibit longer residence times in the order of 30–45 min and grow at much slower rates of less than $5 \times 10^{-3} \text{ mm min}^{-1}$. While bubble α appears to shrink in Figure 11a, it is in fact slowly growing while its center of mass is moving deeper into the FOV; consequently, this two dimensional tomograph

captures a smaller slice through a larger total bubble volume, thus highlighting the importance of using three-dimensional analysis to characterize the bubble population. In general, the smaller bubbles are observed to grow most quickly, consistent with the square root time dependency of diffusion controlled bubble growth in Eq. 12. However, there is substantial variation in the growth rate of similar sized bubbles at different locations in the sediment. A more thorough investigation of bubble growth kinetics would require a modified CT configuration which enables shorter time intervals between scans.

The slow and decelerating rise of the bubbles labeled “ α ” and “ β ” is considered to be a result of their movement in conjunction with the bulk sediment due to bed expansion, rather than their rise through the sediment by fluidization, as the rise rates correlate closely with bed expansion rates. The stability of bubble α within the sediment over the initial 45 min period implies a critical bubble diameter greater than 3.6 mm, corresponding to the d_{60} bubble diameter in Figure 10a. Conversely, the absence of bubble β from the 60-min tomograph suggests that this 1.6 mm bubble is able to fluidize the bed between the 45 and 60 min frames, thus implying a smaller critical rise diameter.

Atapattu et al.¹⁸ have demonstrated a significant history dependence of creeping sphere motion within non-Newtonian Herschel-Bulkley fluids, where spheres were shown to exhibit elevated terminal velocities after a series of repeat experiments, suggesting that the disturbed fluid behaves with a lower observed viscosity than the undisturbed fluid. This hysteresis effect, combined with some spatial heterogeneity in the sediment mechanics, implies that the critical rise diameter exhibits both time and position dependence. The same observation also means that the viscous resistance to bubble growth is spatially and temporally dependent and so growth rates for bubbles of equivalent size may vary greatly even if the material is uniformly supersaturated with volatiles. However, despite the

Table 2. Contribution of the Observable ($d_b > 0.83$ mm) and Subresolution Bubble Populations to the Total Voidage

τ (Pa)	v	V_R (mL)	$V_{R, \text{tom}}$ (mL)	$100 \times v_{\text{tom}}$ (%)
7	0.32	2188	0.616	0.03
86	0.29	1829	16.9	0.92
234	0.34	2325	25.1	1.08
1112	0.24	1467	110	7.50

considerable spacial variation in bubble growth rate and likely spacial variation in local yield stress, the fact that the largest bubbles within the small FOV of the 7 Pa sediment, with the largest buoyant force, exhibit the longest residence times in the bed implies that bubble fluidization of the bed, as represented by Eq. 11,^{9,18} is not the dominant mechanism of gas release, even from this very low strength sediment.

Further evidence that fluidization is unlikely to explain the rates of gas release observed in Figure 6b lies in the fact that the mature, observable bubble population represents a small percentage of the total voidage. The average voidage of the bed can be estimated from the bed swell observed in profile *scout* tomographs of the whole bed, as presented in Figure 8a, and hence the total volume of free gas within the large FOV tomographs can be attained. Table 2 compares the total volume of free gas within the large FOV, V_R , with the total volume of the *observable* bubble population, $V_{R, \text{tom}}$, obtained using three-dimensional image analysis of tomographs such as those presented in Figure 9. The volume of the observable population captures the bubbles greater than 0.83 mm equivalent spherical diameter but excludes any bubbles or fractures extending to the edge of the FOV. The ratio of bubbles observable at the tomography resolution, $v_{\text{tom}} = \frac{V_{R, \text{tom}}}{V_R}$, varies between 0.03 and 1.08% for 7–234 Pa yield stress sediments, rising to 7.5% for the highest strength bed (1112 Pa).

This very small contribution of millimeter scale bubbles to the total voidage, especially within the low strength sediments, suggests that the dominant gas release mechanism is unlikely to be buoyancy driven. Other possibilities for gas release include gas diffusion through subresolution channels or *dendritic* bubble networks, or direct mass transfer of dissolved oxygen through the surface of the bed to the ullage. The rate at which aqueous oxygen is transferred through the liquid and gas films at the bed boundary, $\dot{V}_{E, \text{aq}}$, can be estimated using two-film theory,⁵⁹ by assuming both phases are well mixed, combined with the ideal gas law

$$\dot{V}_{E, \text{aq}} = \frac{RT}{P} JA = \frac{RT}{P} KA \frac{(c_{O_2}(\text{aq}) - \frac{p_{O_2}}{H^{pc}})}{H^{cc}} \quad (15)$$

where J is molar flux of oxygen through the surface of the bed, A is the surface area of the bed, K is the overall mass transfer coefficient, and H^{pc} and H^{cc} are dimensional and dimensionless forms of the Henry's law constant for oxygen in water, respectively. The liquid side mass transfer resistance is reported to be negligible for the exchange of pollutants between air and water and so the overall coefficient approximates that through the gas film, $K \approx k_g$.⁵⁹ The gas side mass transfer coefficient can be estimated from the Froessling equation,⁶⁰ which states that the Sherwood number, $Sh = \frac{KD}{k_g}$, tends to 2 for a stagnant ullage where $Re \rightarrow 0$.

Considering the gas retention test in Figure 6b, the diffusion coefficient of $1.76 \times 10^{-5} \text{ m}^2 \text{ s}^{-1}$ for oxygen in air and the characteristic length scale, l , equal to the 0.118 m test vessel diameter, provides a mass transfer coefficient of $2.98 \times 10^{-4} \text{ m}$

s^{-1} . Thus, assuming the pore water was saturated at the maximum possible oxygen concentration of $2.99 \times 10^{-2} \text{ M}$, oxygen transport to the ullage would be limited to 0.27 mL h^{-1} , representing only 0.13% of the observed rate of gas release. Consequently, it appears that gas release from these low strength soft sediments, in the absence of a supernatant, is governed overwhelmingly by transport of free gas at a subresolution length-scale, possibly along networks of dendritic bubbles. Such a gas release mechanism would accord with the observation that coarse grained sediments which promote bubble growth into adjacent pore space by capillary invasion typically exhibit lower maximum void fractions than sediments in which bubbles grow predominantly by elastic cavity expansion.⁴⁴ Clinical x-ray CT is available at greater resolution, of around 50 mm, for experimentation at a reduced scale and work is ongoing to investigate bubble growth and gas transport closer to the pore scale using this technique.

The growth and motion of retained bubbles is more apparent in Figure 11b, as bubbles reside over much longer periods within the high strength 1112 Pa sediment. Large FOV tomographs at 0, 2, and 6 h demonstrate both the bulk expansion of the bed (from black to green to orange) within the sideways mounted cylinder and the growth and movement of bubbles during this period. The inverted teardrop bubble, ζ' , of 8.9 mm equivalent spherical diameter, is visible within all three time frames, moving in tandem with the local sediment due to bed expansion. During the 6 h of gas generation, the maximum dimension of ζ increases from 12 to 19 mm and the bubble tail narrows to a thin point, similar to phenomena described in Algar et al.³⁷ The stability of the largest bubbles of 8–20 mm equivalent spherical diameter on a timescale of hours confirms that fluidization does not play a significant role in gas release in soft sediments in excess of 1 kPa yield stress. Nonetheless, the rate of gas release from this bed exceeds that from each of the lower strength sediments investigated. Gas transport from the bed is better explained by diffusion along cracks such as those labeled “ δ ,” “ ϵ ,” and “ η ,” especially in the instance of bubble η , as this fracture extends to the periphery of the bed. These lateral cracks are more prevalent within the 2 and 6 h tomographs than at 0 h, indicating that only fairly mature bubbles acquire the excess bubble pressures necessary for tensile fracture. Cracks δ and ϵ fall in their positions within the FOV between 2 and 6 h, and hence these local regions of the bed undergo compression while other regions continue to expand. The high radiodensity, high strength, and deeper regions, often associated with reduced Poisson ratios,^{9,14} in Figures 9d and 11b, appear to be more prone to consolidation and exhibit more growth by tensile fracture than viscoelastic cavity expansion.

All x-ray CT presented and analysed in Figures 8–11 used *in situ* gas generation by injecting hydrogen peroxide at the sample homogenization stage, to achieve a relatively uniform distribution of the gas generating reagent. Figure 7, however, revealed a significant reduction in the bulk bed expansion using an alternative methodology (where the peroxide was injected into the feed line at a constant rate) which manifested in an assumed more heterogeneous distribution of hydrogen peroxide through the bed (evidenced from the lower and more varied total gas hold-up). The reason for this disparity is investigated in Figure 12, using x-ray CT of a 7 Pa sediment 6 h after hydrogen peroxide introduction at Stage 2 in Figure 2. The different approach to gas generation is marked by two features within the bed, which are distinct from the otherwise

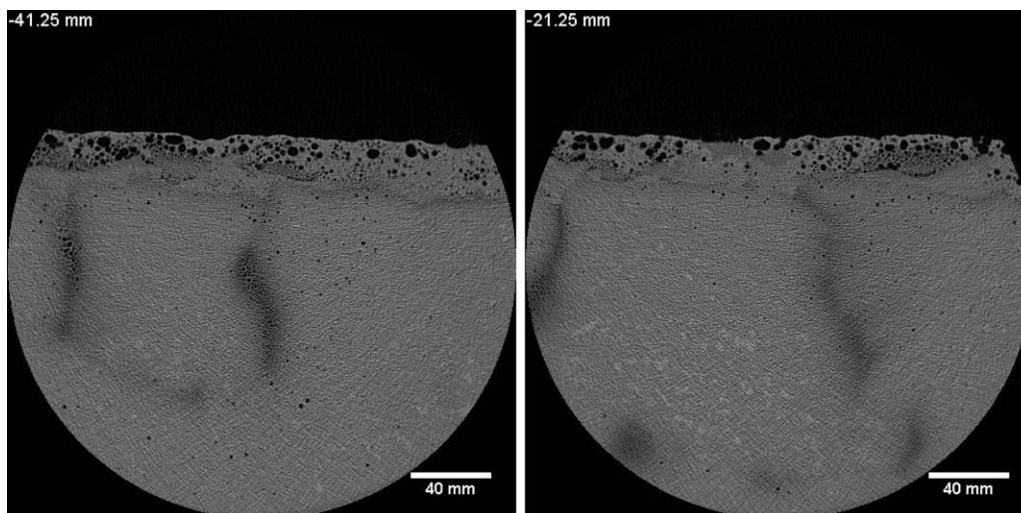


Figure 12. X-ray tomographs at two depths within the large FOV of 7 Pa sediment after 6 h gas generation following hydrogen peroxide addition at injection point 2 (Figure 2).

identical bed of equivalent yield stress imaged in Figure 9a. First, the bed segregates into a bulk sediment and a foam layer which covers the top 20–30 mm of the bed. The foam layer supports a much greater void fraction than the bulk sediment and includes much larger, less spherical bubbles, often separated by very thin particle films. The formation of this foam layer implies that a portion of solids in the bed have a three-phase contact angle greater than zero, while Hunter et al.⁶¹ suggest that three phase contact angles of at least 40° are typically required to stabilize bubbles within a foam. One significance of this layer is that the foam would become unstable in the presence of an aqueous supernatant; it is likely that this foam layer would rise through the supernatant and some of the solid material in the foam would be supported at the top of the convective waste layer as a floating crust, as observed in certain underground waste tanks at Hanford.^{11,40}

Second, a series of dark streaks propagating through the bulk sediment below the foam layer in Figure 12 reveal low radiodensity regions, rich with microbubbles close to the pixel resolution. The poor distribution of hydrogen peroxide through the bed is believed to result in regions of above average oxygen supersaturation and a greater bubble nucleation rate. Enhanced gas transport through these low density, low strength regions to the walls of the test cylinder and the foam layer could explain the augmented rate of gas release from the bed in Figure 12, resulting in the lower maximum voidage of just 6.8% in comparison to that of 31.8% observed in Figure 9a. Hence, these gas transport pathways could represent an alternative mechanism for gas release from heterogeneous soft sediments, distinct from the stable open channels discussed in van Kessel and van Kesteren,⁹ which are visible at the bed surface and are characteristic of beds with much greater yield stress. The two tomographs at different axial depths demonstrate these submerged pathways propagating at multiple locations and along multiple directions through the bed. Enhanced gas transport along these pathways to the weakly consolidated top region of the bed could facilitate formation of the stable foam layer, which is not observed within the equivalent 7 Pa sediment in Figure 9a. It is noted additionally that such gas transport pathways may indeed be relatively common in corroding nuclear wastes, as flammable gas generation would be thought of as inherently inhomogeneous in these systems, as it

would be focused in localized areas with exposed corroding metallic fuel debris.

Conclusions

Understanding the mechanisms for growth and release of bubbles from soft sediments is critical to mitigating the risk of large periodic releases of flammable gas from radioactive waste facilities, including those at Sellafield, UK and Hanford, USA. A series of laboratory scale gas retention tests have demonstrated the capacity of sediments up to 800 Pa yield stress to retain a large voidage of gas, in the order of 30%, sufficient to enable the rollover events that trigger acute gas releases. X-ray computed tomography has revealed that the size distribution of mature bubbles remains constant after less than an hour of gas generation, long before the cessation of bed expansion and the exhaustion of gas production. The absence of bubble coarsening could be explained by a combination of the exponentially diminishing oxygen source strength and by reductions in the oxygen concentration gradient due to the rise in internal bubble pressure as a result of the sediments' elastic resistance to bubble growth.

Mature bubbles of greater than 3.6 mm diameter are observed to grow with greater aspect ratios, or reduced sphericity, in sediments of greater yield stress, explained by greater anisotropy in stress tensors within the more consolidated beds. The highest strength sediment ($\tau = 1112$ Pa) supported laterally oriented cracks consistent with bubble growth by tensile fracture. Diffusion of volatiles along these fracture sites to the bed periphery would explain the reduced void fractions observed in sediments of greater than 800 Pa yield stress. For weak-intermediate strength sediments ($\tau = 7-234$ Pa) our results suggest the presence of a novel gas release mechanism, as the majority of gas release cannot be explained by existing mechanisms: acute release from partial or full rollover, diffusion of aqueous volatiles, and fluidization by mature discrete bubbles. The majority of gas release is therefore governed by transport of free gas at submillimeter length scales. It is unclear whether these are in the form of discrete channels or dendritic bubble networks below the resolution of the CT scanner.

Nonhomogeneous distribution of volatiles through the sediments produced localized pockets of gas generation which

resulted in low density regions rich with microbubbles. Gas transport along these low-density pathways offers the best explanation for the enhanced rate of continuous gas release from soft-sediments experiencing heterogeneous *in situ* gas generation. It therefore appears that mobilizing, diluting, and homogenizing these highly consolidated beds for transport from aging facilities will likely increase their capacity to retain large void fractions of hydrogen and so steps should be taken to mitigate the risk of buoyant rollover. These measures could entail dewatering these sediments back to high yield stress conditions which inhibit substantial gas accumulation within the bed, by shielding radiation using means other than an aqueous supernatant, or by the provision of sufficient tank ullage capacity such that the lower flammability limit is not attained in the event of acute gas release.

Acknowledgments

The authors wish to thank the anonymous reviewers for their invaluable contribution to this research. Thanks also go to the Nuclear Decommissioning Authority (NDA) and Sellafield Ltd. for funding this work through an Engineering and Physical Sciences Research Council (EPSRC) industrial case award (Grant EP/K504440). We also thank Geoff Randall and Martyn Barnes of Sellafield Ltd. for their support of this research, Samuel Allshorn and Carlos Grattoni of the University of Leeds Wolfson Laboratory for hosting the x-ray tomography component of this research, and Tony Windross for manufacturing the experimental rigs used throughout this study.

Literature Cited

- Johnson BD, Boudreau BP, Gardiner BS, Maass R. Mechanical response of sediments to bubble growth. *Mar Geol.* 2002;187:347–363.
- Boudreau BP, Algar C, Johnson BD, Croudace I, Reed A, Furukawa Y, Dorgan KM, Jumars PA, Grader AS, Gardiner BS. Bubble growth and rise in soft sediments. *Geology.* 2005;33:517–520.
- Katsman R, Ostrovsky I, Makovsky Y. Methane bubble growth in fine-grained muddy aquatic sediment: insight from modeling. *Earth Planet Sci Lett.* 2013;377–378:336–346.
- Jain AK, Juanes R. Preferential mode of gas invasion in sediments: grain-scale mechanistic model of coupled multiphase fluid flow and sediment mechanics. *J Geophys Res Solid Earth.* 2009;114(B8).
- Wheeler S. A conceptual model for soils containing large gas bubbles. *Geotechnique.* 1988;38:389–397.
- Keller M, Stallard RF. Methane emission by bubbling from Gatun Lake, Panama. *J Geophys Res Atmos.* 1994;99:8307–8319.
- Winterwerp J, van Kesteren WGM. *Introduction to the Physics of Cohesive Sediment Dynamics in the Marine Environment*, Vol. 56. Amsterdam, The Netherlands: Elsevier, 2004.
- Sills G, Gonzalez R. Consolidation of naturally gassy soft soil. *Geotechnique.* 2001;51:629–639.
- van Kessel T, van Kesteren WGM. Gas production and transport in artificial sludge depots. *Waste Manag.* 2002;22:19–28.
- Jolly M, Belshaw D, Telfer J. The biochemical relationships in anaerobic digestion after thermal hydrolysis at Davyhulme. *Water Environ J.* 2014;28:459–472.
- Bryan S, Pederson L, Scheele R. Crust growth and gas retention in synthetic Hanford waste, Paper presented at: Waste Management, Tucson, AR, 1992.
- Kam SI, Gauglitz PA, Rossen WR. Effective compressibility of a bubbly slurry. I. Theory of the behavior of bubbles trapped in porous media. *J Colloid Interface Sci.* 2001;241:248–259.
- Kam SI, Gauglitz PA, Rossen WR. Effective compressibility of a bubbly slurry. II. Fitting numerical results to field data and implications. *J Colloid Interface Sci.* 2001;241:260–268.
- Terrones G, Gauglitz PA. Deformation of a spherical bubble in soft solid media under external pressure. *Q J Mech Appl Math.* 2003;56: 513–525.
- Gregson CR, Goddard DT, Sarsfield MJ, Taylor RJ. Combined electron microscopy and vibrational spectroscopy study of corroded Magnox sludge from a legacy spent nuclear fuel storage pond. *J Nucl Mater.* 2011;412:145–156.
- Hastings JJ, Rhodes D, Fellerman AS, McKendrick D, Dixon C. New approaches for sludge management in the nuclear industry. *Powder Technol.* 2007;174:18–24.
- Kam SI, Gauglitz PA, Rossen WR. The yield stress of foamy sands. *Colloids Surf A Physicochem Eng Aspects.* 2002;202:53–62.
- Atapattu D, Chhabra R, Uhlherr P. Creeping sphere motion in Herschel-Bulkley fluids: flow field and drag. *J Non-Newtonian Fluid Mech.* 1995;59:245–265.
- Ransohoff TC, Gauglitz PA, Radke CJ. Snap-off of gas bubbles in smoothly constricted noncircular capillaries. *AIChE J.* 1987;33:753–765.
- Rossen WR, Gauglitz PA. Percolation theory of creation and mobilization of foams in porous media. *AIChE J.* 1990;36:1176–1188.
- Gauglitz PA, St. Laurent CM, Radke CJ. Experimental determination of gas-bubble breakup in a constricted cylindrical capillary. *Ind Eng Chem Res.* 1988;27:1282–1291.
- Ali SA, Gauglitz PA, Rossen WR. Stability of solids-coated liquid layers between bubbles. *Ind Eng Chem Res.* 2000;39:2742–2745.
- Gauglitz PA, Friedmann F, Kam SI, Rossen WR. Foam generation in homogeneous porous media. *Chem Eng Sci.* 2002;57:4037–4052.
- Nguyen QD, Boger DV. Application of rheology to solving tailings disposal problems. *Int J Miner Process.* 1998;54:217–233.
- Seysiecq I, Ferrasse JH, Roche N. State-of-the-art: rheological characterisation of wastewater treatment sludge. *Biochem Eng J.* 2003; 16:41–56.
- Chang C, Smith PA. Rheological characterization of nuclear waste slurries. *Part Sci Technol.* 1996;14:165–180.
- Boger DV. Rheology of slurries and environmental impacts in the mining industry. *Annu Rev Chem Biomol Eng.* 2013;4:239–257.
- Boger DV. Rheology and the resource industries. *Chem Eng Sci.* 2009;64:4525–4536.
- Jeldres RI, Toledo PG, Concha F, Stickland AD, Usher SP, Scales PJ. Impact of seawater salts on the viscoelastic behavior of flocculated mineral suspensions. *Colloids Surf A Physicochem Eng Aspects.* 2014;461:295–302.
- Goñi C, Jeldres RI, Toledo PG, Stickland AD, Scales PJ. A non-linear viscoelastic model for sediments flocculated in the presence of seawater salts. *Colloids Surf A Physicochem Eng Aspects.* 2015;482: 500–506.
- Weertman J. Theory of water-filled crevasses in glaciers applied to vertical magma transport beneath oceanic ridges. *J Geophys Res.* 1971;76:1171–1183.
- Takada A. Experimental study on propagation of liquid-filled crack in gelatin: Shape and velocity in hydrostatic stress condition. *J Geophys Res Solid Earth.* 1990;95:8471–8481.
- Wheeler S, Gardner T. Elastic moduli of soils containing large gas bubbles. *Geotechnique.* 1989;39:333–342.
- Boudreau BP. The physics of bubbles in surficial, soft, cohesive sediments. *Mar Pet Geol.* 2012;38:1–18.
- Schindelin J, Arganda-Carreras I, Frise E, Kaynig V, Longair M, Pietzsch T, Preibisch S, Rueden C, Saalfeld S, Schmid B, Tinevez JY. Fiji: an open-source platform for biological-image analysis. *Nat Methods.* 2012;9:676–682.
- Algar CK, Boudreau BP. Stability of bubbles in a linear elastic medium: implications for bubble growth in marine sediments. *J Geophys Res Earth Surface.* 2010;115(F3).
- Algar CK, Boudreau BP, Barry MA. Initial rise of bubbles in cohesive sediments by a process of viscoelastic fracture. *J Geophys Res Solid Earth.* 2011;116(B4).
- Gardiner BS, Boudreau BP, Johnson BD. Growth of disk-shaped bubbles in sediments. *Geochimica Et Cosmochimica Acta.* 2003;67: 1485–1494.
- Katsman R. Correlation of shape and size of methane bubbles in fine-grained muddy aquatic sediments with sediment fracture toughness. *J Struct Geol.* 2015;70:56–64.
- Kam SI, Rossen WR. Anomalous capillary pressure, stress, and stability of solids-coated bubbles. *J Colloid Interface Sci.* 1999;213: 329–339.
- Burrows R, Harris R, Stevens N. Corrosion electrochemistry of fuel element materials in pond storage conditions. *Chem Eng Res Design.* 2005;83:887–892.

42. McCracken G, Eilbeck M. Clean up progress on high hazard facilities at Sellafield: Magnox swarf storage silos. Paper presented at: ANS Topical Meeting on Decommissioning, Decontamination, and Reutilization. August 7–11 2005. Denver, CO. pp. 161–167.
43. Dorgan KM, Jumars PA, Johnson B, Boudreau BP, Landis E. Burrow extension by crack propagation. *Nature*. 2005;433:475.
44. Gauglitz PA, Bontha JR, Daniel RC, Mahoney LA, Rassat SD, Wells BE, Bao J, Boeringa GK, Buchmiller WC, Burns CA. *Hydrogen gas retention and release from WTP vessels: summary of preliminary studies (PNNL tech. rep. no. 24255)*; 2015.
45. Allemann RT. Physical mechanisms contributing to the episodic gas release from Hanford tank 241-SY-101. Paper presented at: ANS International High Level Radioactive Waste Management. April 12-16 1992. Las Vegas, NV.
46. Hunter T, Biggs S, Young J, Fairweather M, Peakall J. Ultrasonic techniques for the in situ characterisation of nuclear waste sludges. Paper presented at: Waste Management. February 27-March 3 2011. Phoenix, AR.
47. Martin Marietta Magnesia Specialties, Versamag magnesium hydroxide safety data sheet. magnesiasspecialties.com. 2014. web access 1 Nov. 2016.
48. Johnson M, Peakall J, Fairweather M, Biggs SR, Harbottle D, Hunter TN. Characterisation of multiple hindered settling regimes in aggregated mineral suspensions. *Ind Eng Chem Res*. 2016;55:9983–9993.
49. Dzuy NQ, Boger DV. Direct yield stress measurement with the vane method. *J Rheol*. 1985;29:335–347.
50. Barnes HA. The yield stress – a review or $\pi\alpha\tau\alpha\rho\epsilon\iota$ – everything flows? *J Non-Newtonian Fluid Mech*. 1999;81:133–178.
51. Uhlherr PHT, Guo J, Tiu C, Zhang XM, Zhou JZQ, Fang TN. The shear-induced solid-liquid transition in yield stress materials with chemically different structures. *J Non-Newtonian Fluid Mech*. 2005; 125:101–119.
52. Bolte S, Cordelières F. A guided tour into subcellular colocalization analysis in light microscopy. *J Microsc*. 2006;224:213–232.
53. Kapur JN, Sahoo PK, Wong AK. A new method for gray-level picture thresholding using the entropy of the histogram. *Comput Vis Graph Image Process*. 1985;29:273–285.
54. Nguyen QD, Boger DV. Measuring the flow properties of yield stress fluids. *Annu Rev Fluid Mech*. 1992;24:47–88.
55. Bird BR, Dai G, Yarusso BJ. The rheology and flow of viscoplastic materials. *Rev Chem Eng*. 1983;1:1–70.
56. Liddell PV, Boger DV. Yield stress measurements with the vane. *J Non-Newtonian Fluid Mech*. 1996;63:235–261.
57. Boudreau BP, Gardiner BS, Johnson BD. Rate of growth of isolated bubbles in sediments with a diagenetic source of methane. *Limnol Oceanogr*. 2001;46:616–622.
58. Bowers PG, Hofstetter C, Letter CR, Toomey RT. Supersaturation limit for homogeneous nucleation of oxygen bubbles in water at elevated pressure: Superhenry's law. *J Phys Chem*. 1995;99:9632–9637.
59. Ibusuki T, Aneja VP. Mass transfer of NH_3 into water at environmental concentrations. *Chem Eng Sci*. 1984;39:1143–1155.
60. Froessling N. Über die verdunstung fallender tropfen. *Gerlands Beiträge Zur Geophysik*. 1938;52:170–215.
61. Hunter TN, Wanless EJ, Jameson GJ. Effect of esterically bonded agents on the monolayer structure and foamability of nano-silica. *Colloids Surf A Physicochem Eng Aspects*. 2009;334:181–190.

Manuscript received Nov. 2, 2016, and revision received Mar. 9, 2017.